AGU PUBLICATIONS

JGR

Journal of Geophysical Research: Oceans

RESEARCH ARTICLE

10.1002/2016JC012187

Special Section:
Atmosphere-ice-ocean-ecosystem Processes in a Thinner Arctic Sea Ice Regime: The Norwegian Young Sea ICE Cruise 2015 (N-ICE2015)

Effects of an Arctic under-ice bloom on solar radiant heating of the water column

Torbjørn Taskjelle[1], Mats A. Granskog[2], Alexey K. Pavlov[2], Stephen R. Hudson[2], and Børge Hamre[1]

[1]Department of Physics and Technology, University of Bergen, Bergen, Norway, [2]Norwegian Polar Institute, Fram Centre, Tromsø, Norway

Abstract The deposition of solar energy in the upper Arctic Ocean depends, among other things, on the composition of the water column. During the N-ICE2015 expedition, a drift in the Arctic pack ice north of Svalbard, an under-ice phytoplankton bloom was encountered in May 2015. This bloom led to significant changes in the inherent optical properties (IOPs) of the upper ocean. Mean values of total water absorption in the upper 20 m of the water column were up to 4 times higher during the bloom than prior to it. The total water attenuation coefficient increased by a factor of up to around 7. Radiative transfer modeling, with measured IOPs as input, has been performed with a coupled atmosphere-ice-ocean model. Simulations are used to investigate the change in depth-dependent solar heating of the ocean after the onset of the bloom, for wavelengths in the region 350–700 nm. Effects of clouds, sea ice cover, solar zenith angle, as well as the average cosine for scattering of the ocean inclusions are evaluated. An increase in energy absorption in the upper 10 m of about 36% is found under 25 cm ice with 2 cm snow, for bloom conditions relative to pre-bloom conditions, which may have implications for ice melt and growth in spring. Thicker clouds and lower sun reduce the irradiance available, but lead to an increase in relative absorption.

Key Points:
- Phytoplankton bloom caused up to 4 (7) times higher total water absorption (attenuation)
- Radiative transfer modeling suggests energy deposition in the upper 10 m increased by about 35%
- Over 25 days, bloom could cause additional 0.2 K solar warming of the upper 10 m

Correspondence to:
T. Taskjelle,
torbjorn.taskjelle@uib.no

Citation:
Taskjelle, T., M. A. Granskog, A. K. Pavlov, S. R. Hudson, and B. Hamre (2017), Effects of an Arctic under-ice bloom on solar radiant heating of the water column, *J. Geophys. Res. Oceans*, *122*, 126–138, doi:10.1002/2016JC012187.

Received 28 JUL 2016
Accepted 30 OCT 2016
Accepted article online 7 NOV 2016
Published online 11 JAN 2017

1. Introduction

The fate of the sunlight incident on the sea ice covered Arctic Ocean depends on many factors. Given the high albedo of snow covered sea ice [e.g., *Grenfell and Perovich*, 1984], the state of the ice and snow cover itself is the dominating factor. However, as some light will pass through the ice, the properties of the water column below the ice also have bearing on where the solar energy ends up [*Pegau*, 2002]. The Arctic Ocean is also moving to a regime with thinner ice, and possibly more open leads, which will increase the energy input in the upper ocean [*Arndt and Nicolaus*, 2014]. Prevalence of particulate (including plankton) and dissolved matter in the water will modify the absorption and scattering properties of the water body, and hence affect the vertical distribution of radiant heating [*Pegau*, 2002; *Granskog et al*., 2015]. In turn, this can affect ice melt if the heat accumulates in the surface mixed layer [*Hudson et al*., 2013; *Granskog et al*., 2015].

The Norwegian Young Sea Ice Experiment (N-ICE2015) was a field campaign lasting from January to June 2015, where the vessel R/V Lance was moored to a total of four ice floes during the expedition [*Granskog et al*., 2016]. An under-ice spring bloom of phytoplankton was encountered over the Yermak Plateau [*Assmy et al*., 2016], during the 7 week drift with the third floe, from mid-April to early June. The bloom appeared to have formed under the ice cover, and continued to develop during N-ICE2015, also being observed during the drift of floe 4. The encounter with the bloom coincided with notable changes in oceanographic conditions [*Meyer et al*., 2016], and caused significant changes in the inherent optical properties (IOPs) of the upper ocean [*Pavlov et al*., 2016]. Under-ice blooms in the high-Arctic have been observed previously, though later in the season [*Pegau*, 2002], under melt-pond covered ice [*Arrigo et al*., 2012], snow-free ice [*Fortier et al*., 2002], or by the ice-edge [*Mundy et al*., 2009]. The bloom encountered during N-ICE2015, however, developed early in the season under sea ice that was covered with thick snow everywhere except on newly refrozen leads.

In this work, we use the AccuRT (Geminor Inc., Maplewood, NJ, USA) radiative transfer model to estimate the changes in the vertical distribution of solar heating under ice and in open water, following the change from relatively transparent surface waters before the bloom, to the more turbid waters encountered during the bloom. We compare our results to *Pegau* [2002] and *Granskog et al*. [2015], but in contrast to their open

water studies we will also consider the effect of the sea ice and snow cover. Finally, using information on ice cover (fractions of open water, thin ice, and thick ice) we estimate the aggregate scale solar heating of the upper ocean in the study region.

2. Observations and Methods

2.1. Ice Conditions

Studies of ice thickness and snow depth were performed on the floes and in the surrounding area (A. Rösel, Norwegian Polar Institute, 2016, personal communication). During the drift on floe 3, a bimodal distribution of both sea ice thickness and snow depth was observed in the area around the ice camp. Many recently refrozen leads in the region led to fairly large areas of ice less than 0.5 m thick, though the main mode of the distribution peaked for a thickness of about 1.2 m. Snow was similarly distributed with a main-mode peak at about 0.45 m, and a side mode with snow depths up to 0.1 m, originating from snow covering refrozen leads. In the area around the camp on floe 4, we saw single mode distributions, with mean values of 1.2 and 0.3 m for ice thickness and snow depth, respectively. However, observations during the drift with floe 4 were only carried out on the thicker main floe, and not on the surrounding leads, causing the absence of the side mode.

2.2. Observations

With the exception of a few vertical absorption profiles in the upper ocean, done in January, the majority of optical measurements were done during floe number three (occupied 18 April to 5 June) and four (7–21 June) of N-ICE2015 [*Granskog et al*., 2016]. The bloom we study here was first encountered under floe 3 on 25 May, and persisted under both floes 3 and 4 until the end of the campaign.

Profiles of radiation absorption and attenuation coefficients were measured with an ac-9 (WET Labs, Philomath, OR, USA) which measured absorption and attenuation at nine distinct wavelengths between 412 and 715 nm. Measurements were done in situ during vertical profiles through holes in the ice. Scattering corrections of the ac-9 absorption data were done by subtracting the measured value at 715 nm [*Zaneveld et al*., 1994], or in some cases that at 650 nm. Subtracting the value at 650 nm was done when the absorption at this wavelength was lower than that at 715 nm. Corrections for temperature and salinity were done using coefficients from *Röttgers et al*. [2014]. Due to technical problems with the long cable, only one full depth profile down to 100 m was collected with the ac-9 after the onset of the bloom. Successful short-cable profiles were conducted from the surface down to about 20 m depth. The data set of measured ocean IOPs [*Taskjelle et al*., 2016a] is described in more detail by *Pavlov et al*. [2016].

At the time, the bloom was encountered, measurements of incident, reflected, and under-ice irradiance were performed under two different ice types on floe 3, using Ramses ACC-VIS sensors (TriOS Mess- und Datentechnik GmbH, Rastede, Germany). These sensors are cosine collectors with a wavelength range 350–900 nm. Continuous measurements on floe 3 [*Taskjelle et al*., 2016b] were performed at a fixed location where the ice thickness and snow depth were approximately 1.3 and 0.4 m, respectively. The under-ice downwelling irradiance was measured approximately 30 cm below the ice bottom. To limit light leakage from the hole drilled for the sensor, the ice core was put back in the hole after deploying the sensor, and the snow shoveled back, so snow depth immediately above the sensor was approximately 40 cm.

In addition, a transect across a refrozen lead was repeated approximately every 2 days from 12 May to 3 June, where the ice was found to be 0.2–0.3 m thick with snow depths up to 0.06 m [*Kauko et al*., 2016]. Under-ice downwelling irradiance was measured using an angled arm that extended 1 m away from the 9 cm diameter hole drilled for the sensor. As the ice was less than 30 cm thick, and the sensor was held as close to the ice bottom as possible, the hole will likely not have had any significant influence on the measurements [*Petrich et al*., 2012].

Sea ice transmittance is calculated as the integral of transmitted irradiance over the integral of incident irradiance:

$$\mathcal{T} = \frac{\int E_{\text{transmitted}}(\lambda)\,\mathrm{d}\lambda}{\int E_{\text{incident}}(\lambda)\,\mathrm{d}\lambda}. \tag{1}$$

Values of transmittance given below, for observations or simulations, are integrated over the wavelength range considered, i.e., 350–700 nm. Albedo is calculated similarly, but with reflected instead of transmitted irradiance in the numerator.

2.3. Modeling

To estimate absorption and attenuation coefficients at 350 nm, the measured values from the ac-9 are extrapolated using a linear fit between 412 and 510 nm, similar to the method by *Granskog et al*. [2015]. Measured absorption and scattering coefficients are used as inputs to a radiative transfer model, where the scattering coefficients are calculated by subtracting the measured absorption coefficients from the measured beam attenuation coefficients.

The model used is AccuRT [*Hamre et al*., 2014], a radiative transfer model based on DISORT [*Thomas and Stamnes*, 1999]. This is a coupled atmosphere-snow-ice-ocean plane parallel model that uses the discrete ordinates method to solve the radiative transfer equation. Measured IOPs are added to the lower slab in addition to pure water, below a layer of ice. The ocean is divided into 2 m thick layers, with measured IOPs from the corresponding depths used in each layer, and the Henyey-Greenstein phase function with an asymmetry factor $g = 0.92$ is applied. This asymmetry factor was chosen as it gives a close approximation to Petzold's average-particle phase function [*Mobley*, 1994]. However, as algae cause a high degree of forward scattering [e.g., *Lotsberg et al*., 2007], 0.92 may not be appropriate after the bloom onset. Implications of higher asymmetry factors will be discussed further in section 3.2.

Two different ice types are considered: thick ice with thick snow and thin ice with thin snow, see section 3 for details. Under-ice irradiance spectra measured during N-ICE2015 are used to adjust the properties of the snow and ice cover used in the model. Reproducing the ice properties and downwelling irradiance exactly has not been prioritized, as the purpose of this study is to consider changes between two different regimes of ocean IOPs; however, a reasonably close match is obtained (Figure 1). For each ice type considered, the snow and ice properties are kept constant in all simulations. Simulations without snow and ice, i.e., open ocean, have also been performed.

Unless otherwise specified, the solar zenith angle was set to 60°, which is representative for the time (26 May 2015), and location of the measurements presented in Figure 1. At this time, R/V Lance was at N80°49.2′E8°19.4′.

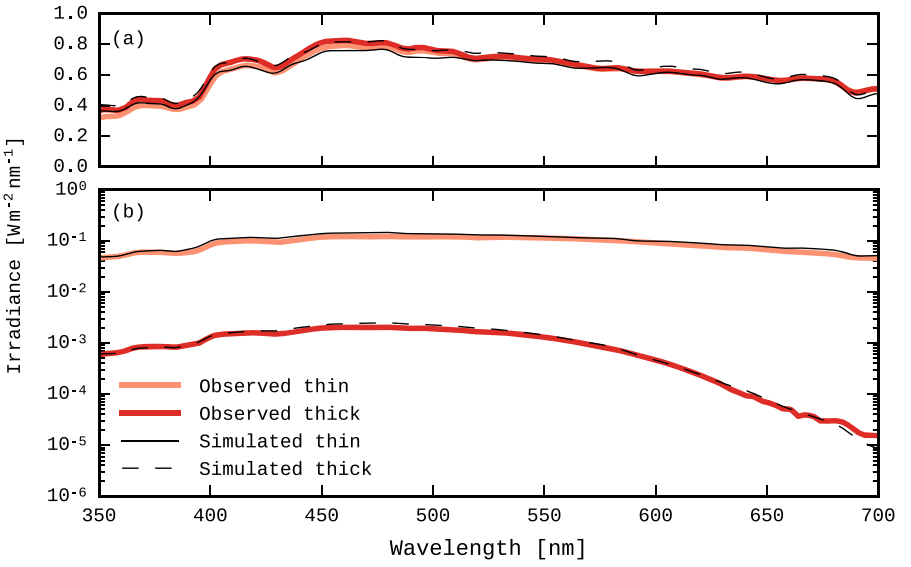

Figure 1. Measured and simulated downwelling planar irradiance. Incident irradiance in Figure 1a, and transmitted irradiance through thick and thin ice in Figure 1b. Note the logarithmic *y* axis in Figure 1b. Measured values are averages of spectra collected between 1200 and 1300 UTC, i.e., early afternoon, on 26 May. The same clouds are used in both simulations, but due to higher albedo for the thick ice case, and multiple reflections between surface and clouds, the simulated values of incident irradiance for thick ice are slightly higher.

Two different cloud conditions are also considered: cloud A is a thin layer of ice clouds that leads to a good representation of the measured incident surface irradiance presented in Figure 1. Cloud base height was set to 500 m, based on measurements done by a Vaisala CL31 ceilometer (V. P. Walden, Washington State University, 2016, personal communication). The thickness of the cloud layer was set to 500 m, particle size to 10 μm, and particle volume fraction adjusted to provide a reasonable match to the measured spectra. Phase function and single scattering albedo are determined through Mie calculations. Compared to a simulation without clouds, incident irradiance is reduced by 22% over the thin ice with snow. Cloud B is an optically thicker cloud layer with the same base height and thickness as cloud A, but higher particle volume fraction. With cloud B, incident irradiance is reduced by 58% compared to clear skies over the same thin ice, which is comparable to some of the lowest irradiance measured near midday during floes 3 and 4.

Simulations cover the wavelengths 350–700 nm, as in the studies by *Pegau* [2002] and *Granskog et al.* [2015]. Further analysis of simulations and plotting was done in Python with libraries `numpy` [*van der Walt et al.*, 2011] and `matplotlib` [*Hunter*, 2007].

Modeled spectral scalar irradiance is used to calculate the heating rate H using Gershun's law [*Mobley*, 2014]:

$$H = a(|E_{\uparrow,0}| + |E_{\downarrow,0}|), \tag{2}$$

where a is the wavelength-dependent total absorption coefficient used by the model in a given layer and $E_{\uparrow,0}$, $E_{\downarrow,0}$ are, respectively, upwelling and downwelling scalar irradiance.

It should be noted that not all light absorbed by phytoplankton contributes directly to heating. *Lin et al.* [2016] estimated that on average 60% of photons absorbed phytoplankton are dissipated to heat in the open ocean. However, not all of the increased absorption in our study is caused by phytoplankton, CDOM absorption in the upper ocean increased as well [*Pavlov et al.*, 2016]. We have made no attempt to separate the effect of phytoplankton, and as such note that the results presented below indicate an upper limit of the heating.

3. Results and Discussion

For transmittance through snow and ice, two cases from 26 May have been selected as baselines to represent the major ice types in the study area. Namely, a thick ice and snow cover (1.3 m ice and 0.4 m snow, hereafter called "thick ice"), and a "thin ice" case from a refrozen lead where ice was 0.25 m thick and had 2 cm of snow, representative of refrozen leads. Incident and transmitted planar irradiance are shown in Figure 1 along with simulated spectra. Simulations were done with 1 nm resolution, and the spectra smoothed with a Gaussian filter ($\sigma = 5$) prior to plotting. A partially broken cloud cover was present on 26 May. Although broken clouds cannot be represented in a 1-D model, the thin ice cloud layer that is used (cloud A, cf. section 2.3), gives a good reproduction of incident irradiance (Figure 1). That the simulated spectra for thick ice is different to that for thin ice, is caused by the difference in albedo, and multiple reflections between surface and clouds. The measured spectra shown in Figure 1 are mean values of spectra collected between 1200 and 1300 UTC. Whether the angular distribution of light is also represented well cannot be determined, as no measurements of radiance or scalar irradiance were conducted.

Figure 2 shows profiles of absorption and attenuation measured by the ac-9 for the wavelengths 440 and 676 nm, before and after encountering the bloom. A deep ac-9 profile from 28 May represents the bloom conditions, while a profile from 9 May represents the prebloom conditions. We see that the prebloom profiles show very little variation with depth. Bloom profiles, especially those for attenuation, show a clearer vertical structure with fairly constant absorption and attenuation in the upper 40 m, then decreasing further down in the water column. These profiles correspond well with the vertical distribution of chlorophyll *a*, showing that the bloom generally extended down to 40 m (P. Assmy, Norwegian Polar Institute, 2016, personal communication). There is also a lot more variability on shorter depth scales ($\sim$1 m) during the bloom than prior to it.

Mean values of total water absorption and attenuation are summarized in Table 1. Values are given for the upper 40 m (for 9 May and 28 May) or upper 20 m (prebloom and bloom mean values). Our prebloom waters show less absorption than any of the cases in the studies by *Pegau* [2002] or *Granskog et al.* [2015],

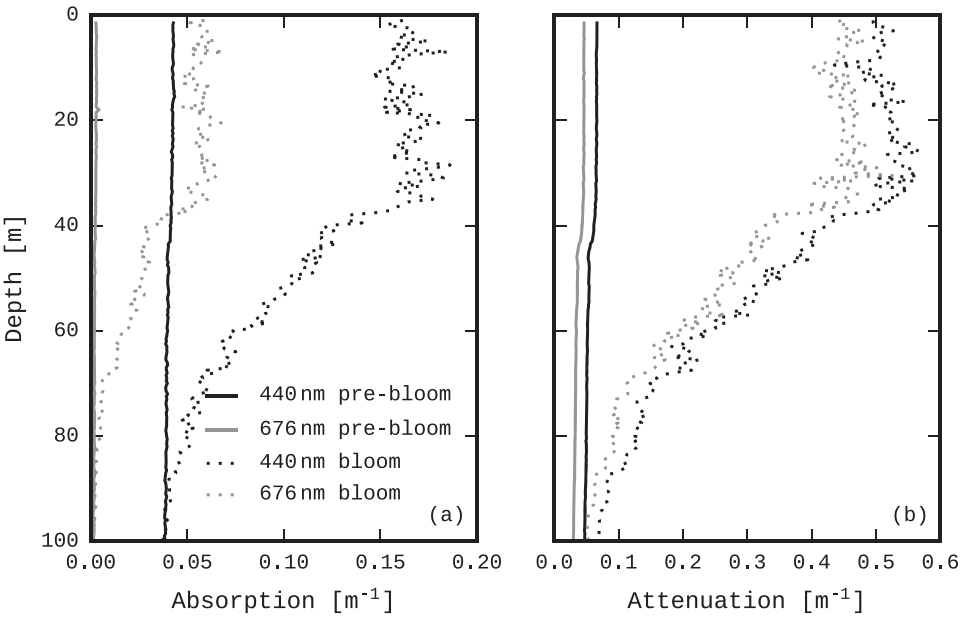

Figure 2. Selected profiles of measured (a) absorption and (b) attenuation coefficients, before (9 May) and after (28 May) bloom onset. Black lines are for 440 nm, grey lines for 676 nm. Solid lines are from 9 May, and dotted lines from 28 May. Absorption by pure water is not included.

which is likely due to low absorption by CDOM during N-ICE2015 [*Pavlov et al*., 2016]. During N-ICE2015 we drifted over Modified Atlantic Water [*Meyer et al*., 2016], which has been seen to have less absorption by CDOM than Polar Waters [*Pavlov et al*., 2015]. As such, the effect of CDOM is perhaps less during N-ICE2015 than in the studies by *Pegau* [2002], *Hill* [2008], and *Hill and Zimmerman* [2016].

Compared to the "turbid" case studied by *Pegau* [2002], the absorption values we observed during the bloom are only slightly higher, but attenuation is more than twice as high. Note that *Pegau* [2002] used values from *Smith and Baker* [1981] for pure water absorption, which are typically higher than those found by *Pope and Fry* [1997] and *Sogandares and Fry* [1997] (up to 0.014 difference, at 350 nm). The mean bloom values are comparable to the case of well mixed surface layers in the West Spitsbergen Current in the study by *Granskog et al*. [2015], but with absorption and attenuation being generally slightly higher in our study.

3.1. Effects of Changes in IOPs on Energy Deposition Under Different Ice and Sky Conditions

Figure 3 shows spectral heating rate *H* under thin ice, thick ice, and open water, calculated for the incident spectra shown in Figure 1. The different scales on the color bars should be noted. Prior to the bloom, the

Table 1. Values of Total Water Absorption (*a*) and Total Water Attenuation (*c*) Used for This Study[a]

	9 May		28 May		Prebloom Mean		Bloom Mean	
Wavelength	*a*	*c*	*a*	*c*	*a*	*c*	*a*	*c*
350[b]	0.118	0.148	0.272	0.616	0.117	0.160	0.267	0.707
412	0.062	0.094	0.178	0.547	0.061	0.106	0.177	0.647
440	0.049	0.077	0.168	0.522	0.049	0.089	0.170	0.624
488	0.026	0.074	0.111	0.503	0.026	0.086	0.116	0.612
510	0.044	0.088	0.101	0.516	0.044	0.100	0.106	0.631
532	0.052	0.100	0.094	0.526	0.052	0.111	0.099	0.641
555	0.065	0.115	0.088	0.541	0.064	0.126	0.093	0.657
650	0.340	0.387	0.354	0.793	0.340	0.397	0.358	0.903
676	0.456	0.500	0.509	0.898	0.457	0.510	0.513	1.004

[a]Absorption [*Pope and Fry*, 1997; *Sogandares and Fry*, 1997] and scattering [*Mobley*, 1994, equation (3)] of pure water are added to the measured values (Figure 2) to obtain total absorption and attenuation. Values from 9 to 28 May are averages of the upper 40 m. prebloom mean is mean of all nine profiles collected before the bloom onset, and bloom mean is a mean of all 25 profiles collected during the bloom, both from the upper 20 m. Both *a* and *c* are given in units of m^{-1}.

[b]Values at 350 nm were extrapolated from observed data, see text.

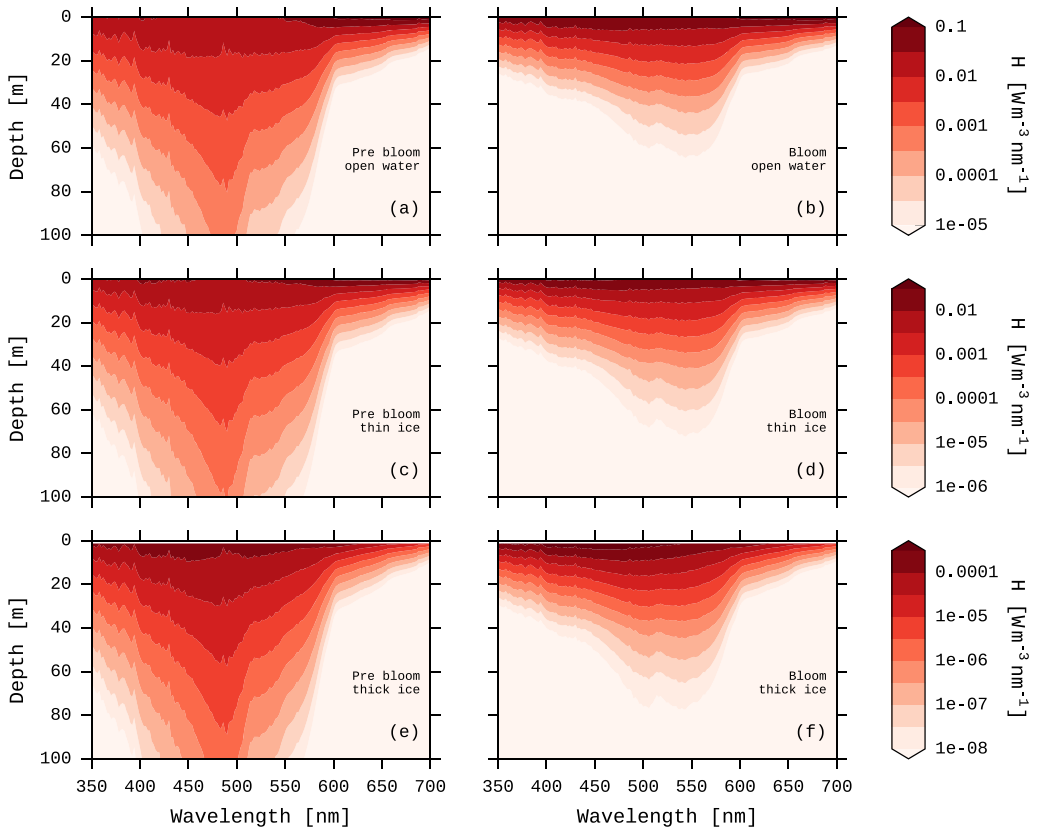

Figure 3. Spectral heating rate in open water (first row), under thin ice (second row), and thick ice (third row). First column shows results for prebloom conditions, second column for bloom conditions. Note separate color bar for each row, with different scales. The underice downwelling irradiance is shown in Figure 1.

energy penetrates deepest in the water column at a wavelength just below 500 nm. After the bloom onset, this wavelength of deepest penetration appears to have shifted to about 550 nm.

Integrating *H* over all wavelengths, we get vertical profiles of absorbed energy, shown in Figure 4 for the upper 30 m. The relative changes in the vertical distribution of the deposition of solar radiation from prebloom to bloom conditions are larger with sea ice present, which is likely due to the absorption of ice. Ice has stronger absorption at the longer wavelengths, which means that the spectral shape of the irradiance entering the water will change, with more irradiance at the shorter wavelengths where the bloom has the strongest absorption. While not apparent from Figure 4, the relative change from prebloom to bloom conditions is also greater when clouds are present, which can be explained by a similar argument: absorption by ice particles in the clouds is greater at the longer wavelengths, which changes the shape of the irradiance spectrum incident on the surface.

The strongest relative effect of the bloom is seen for the thickest ice, with more than twice as much energy being absorbed right below the ice. The same feature is seen when considering the integrated heating over the upper 10 m. Table 2, which summarizes the amount of energy absorbed in the upper 10 m for different ice and sky conditions, shows that the bloom leads to an increase in energy absorption of more than 60% under thick ice. However, even if the relative increase of absorbed energy in the upper few meters is high, the amount of energy passing through the ice is very small. One may also note that the relative change from prebloom to bloom in open water has a maximum at a depth of about 1 m (see also Figure 6a), whereas when ice is present this maximum is immediately below the ice. Both *Pegau* [2002] and *Granskog et al.* [2015] show similar subsurface maxima, but deeper than in this study (depth of 3–5 m).

On interpreting the above results, one should keep in mind that the under-ice light field in the upper ocean cannot be accurately described by a 1-D model in areas with large horizontal gradients in transmittance

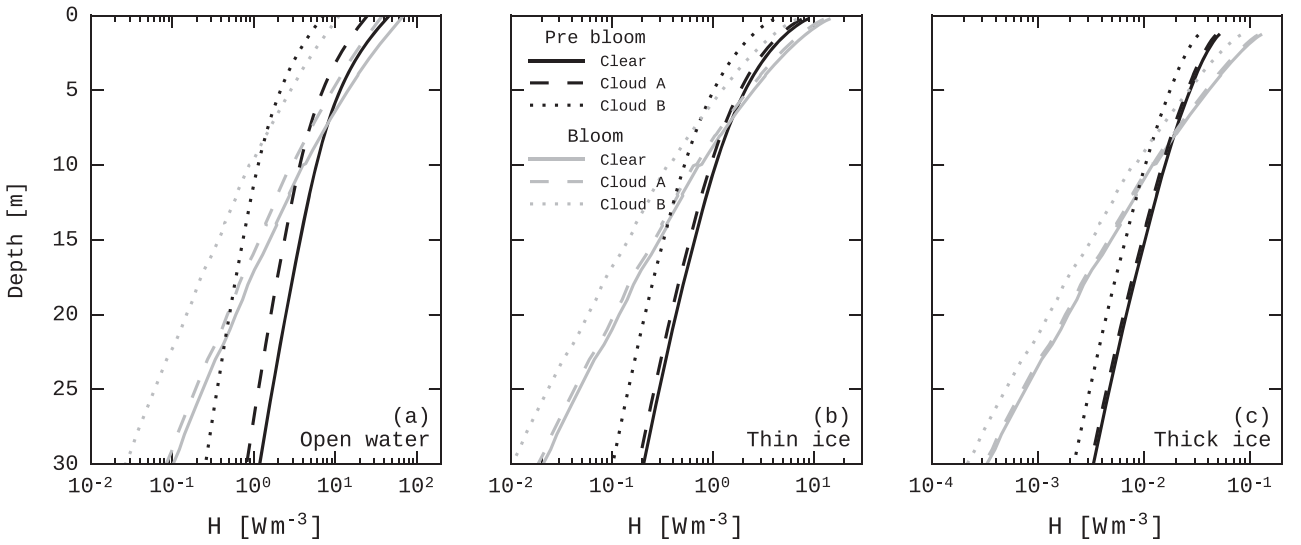

Figure 4. Heating rate as a function of depth during prebloom (black lines) and bloom (grey lines) conditions, for different sky conditions in (a) open water, (b) under thin ice, and (c) under thick ice.

[*Katlein et al.*, 2016]. Therefore, the results are representative only within larger regions with fairly homogeneous ice conditions.

The very high radiation attenuation in the snow cover in particular, results in very low transmittance through the thicker ice type. Hence, the energy input to the upper ocean is 0.5 W m^{-2} under the thick ice, 40 W m^{-2} under the thin ice and 232 W m^{-2} in open water (values from simulations without clouds present, otherwise same settings as in, e.g., Figure 1). This low transmittance through snow-covered ice highlights the importance of leads and regions of young ice when considering the energy input into the Arctic Ocean [e.g., *Perovich*, 2005].

Table 2. Incident Energy and Energy Absorbed in Upper 10 m for Prebloom ($E_{10m,PB}$) and Bloom ($E_{10m,B}$) Conditions, for Different Zenith Angles, Ice Conditions, and Sky Conditions, as Well as the Increase (%) in Absorption in Upper 10 m From Prebloom to Bloom Conditions[a]

	Open Water			Thin Ice			Thick Ice		
Clear									
Zenith angle	60°	70°	80°	60°	70°	80°	60°	70°	80°
Incident (W m^{-2})	247.7	159.3	69.3	270.6	173.1	73.4	274.1	175.2	74.2
$E_{10m,PB}$ (W m^{-2})	154.0	94.0	34.3	26.2	14.8	5.6	0.24	0.13	0.05
$E_{10m,B}$ (W m^{-2})	206.5	125.1	46.3	35.4	20.1	7.7	0.38	0.22	0.09
Increase (%)	34%	33%	35%	35%	36%	38%	61%	62%	63%
Cloud A									
Zenith angle	60°	70°	80°	60°	70°	80°	60°	70°	80°
Incident (W m^{-2})	150.4	85.1	32.5	212.6	120.3	46.0	227.7	128.8	49.3
$E_{10m,PB}$ (W m^{-2})	90.1	50.7	19.1	23.2	13.1	5.0	0.22	0.13	0.05
$E_{10m,B}$ (W m^{-2})	124.4	70.3	26.8	31.5	17.9	6.9	0.36	0.20	0.08
Increase (%)	38%	39%	41%	36%	36%	38%	61%	62%	63%
Cloud B									
Zenith angle	60°	70°	80°	60°	70°	80°	60°	70°	80°
Incident (W m^{-2})	45.4	25.7	9.9	111.8	63.4	24.4	151.1	85.7	33.0
$E_{10m,PB}$ (W m^{-2})	26.9	15.2	5.7	10.8	6.1	2.3	0.11	0.06	0.02
$E_{10m,B}$ (W m^{-2})	37.6	21.3	8.2	15.2	8.7	3.4	0.18	0.10	0.04
Increase (%)	40%	41%	42%	41%	41%	43%	71%	71%	71%

[a]All values are from simulations with AccuRT, integrated over the range 350–700 nm.

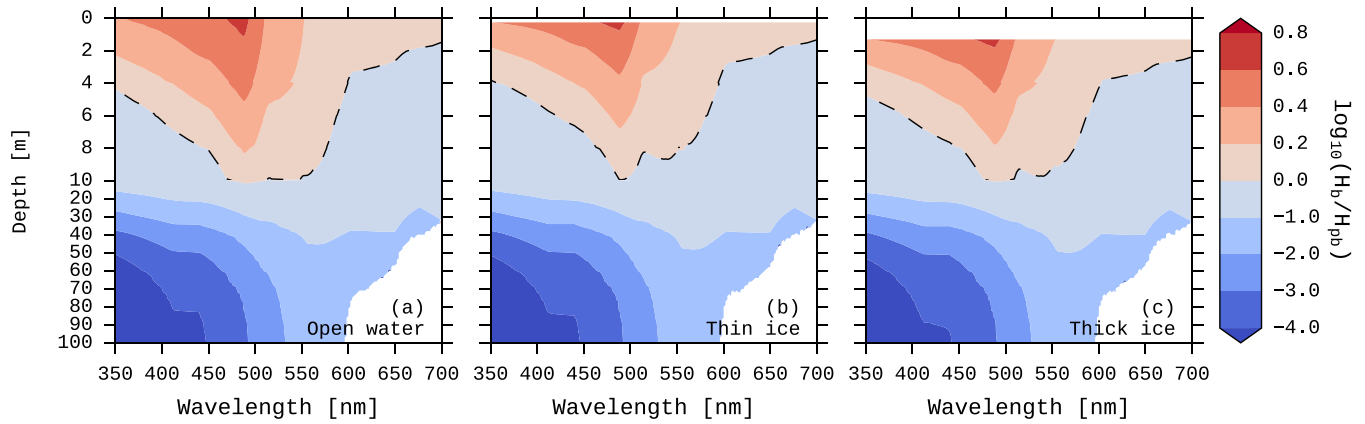

Figure 5. Contour plots of spectral heating rate during bloom conditions compared to prebloom conditions, on a $\log_{10}$ scale. Calculated as $\log_{10}(H_b/H_{pb})$ where H_b and H_{pb} are the spectral heating rates, as shown in Figure 3, for prebloom and bloom conditions, respectively. Note that the colorbar scale is different for positive and negative numbers, and also that the upper 10 m of the *y* axis has a different scale than the lower 90 m. The dashed contours are the zero-contours, i.e., where there is no change in heating rate. Data are from simulations without clouds.

When considering results for ice free conditions, it is also worth mentioning that the increased scattering by the algae has an effect on the albedo. For a zenith angle of 60° and asymmetry factor $g = 0.92$, albedo increases by 4.7%, from 0.074 to 0.078 (integrated values from 350 to 700 nm) under clear skies, meaning that the total energy input to the open ocean decreases slightly with the occurrence of the bloom. With clouds present, albedo increases by 4.2%. Albedo increases further for increasing zenith angle, but the relative importance of the algal particles decrease as specular reflection dominates. Note that AccuRT uses a smooth water surface, so the effect of waves is not taken into account.

Figure 5 shows the spectral dependence of the change in heating rate from simulations without clouds. The plotted values are $\log_{10}(H_b/H_{pb})$, where subscripts indicate bloom and prebloom. Enhanced heating rates extend deepest around 500 nm. The dashed line indicates the depth where the difference in heating rate is zero, so we see that below 10 m depth the water absorbs less heat regardless of wavelength. Beyond 600 nm the absorption by water and ice quickly becomes so high that it completely dominates, though a small effect of the chlorophyll absorption peak at 676 nm can be seen in the contour between 30 and 40 m depth. The white region in the bottom right is where irradiance is below the model numerical threshold, so no relative change can be calculated.

3.2. Asymmetry Factor

As mentioned above, the Henyey-Greenstein phase function was used with an asymmetry factor of 0.92 for scattering by particles in the ocean. Because algae can be very strongly forward scattering, 0.92 is not necessarily an accurate asymmetry factor in bloom conditions, and a different value could be more appropriate. Algae are not the only scattering objects in the water column, so the actual asymmetry factor depends not only on the algae. A study done on various algal species found in Norwegian coastal water found asymmetry factors in the range 0.90–0.99 (B. Hamre, University of Bergen, 2016, personal communication). The study does not, however, include *Phaeocystis pouchetii*, the species dominating the bloom observed during N-ICE2015 [*Assmy et al*., 2016]. Figure 6a shows the relative change in heating rate for a range of different values for *g*. As expected, higher *g* leads to more light being scattered further down the water column, and hence a decrease in heating in the upper layer.

When considering the upper 10 m in bloom (prebloom) conditions, increasing *g* from 0.92 to 0.98 decreases the total energy absorption by about 2.3% (0.9%) under thin ice, and 2.7% (1%) in open ocean. The albedo of open water also depends on *g*. In bloom conditions, increasing *g* from 0.92 to 0.98 decreases the albedo by 9%, from 0.078 to 0.072. For prebloom conditions, the decrease in albedo is less than 2%, from 0.074 to 0.073.

3.3. Zenith Angle Dependence

Under clear skies, as the sun approaches the horizon the ice transmittance will be reduced, because the higher incidence angle causes a larger fraction of the light to be reflected or backscattered. Figure 6b shows the relative effect of bloom on energy deposition with different zenith angles for open ocean and thin ice

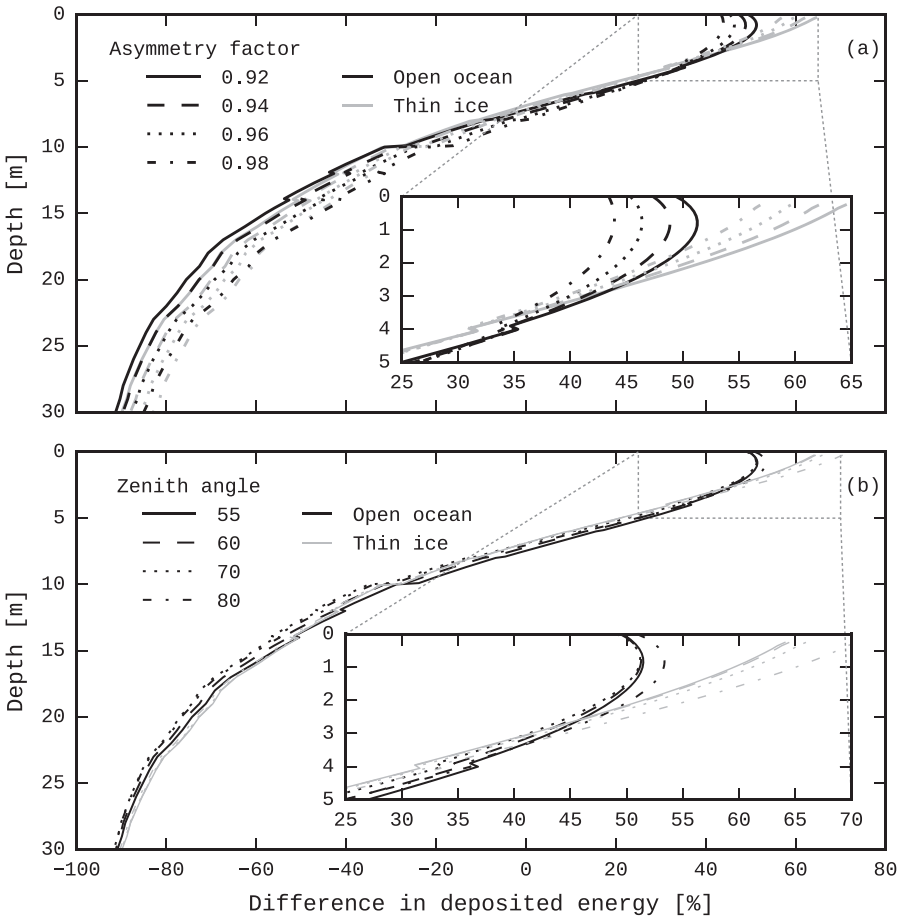

Figure 6. (a) Difference in deposited energy between bloom and prebloom conditions for different values of *g*, without clouds, for open ocean and thin ice cover. (b) Difference in deposited energy between bloom and prebloom conditions for different solar zenith angles without clouds present. In both plots, grey lines are for thin ice and black lines for open ocean.

from prebloom to bloom conditions under clear skies. The lowest value of 55° was chosen as the sun does not go higher during the year at latitudes above 80°. While the average direction of incident light is very different for different zenith angles, directly below the ice there is no such variation; the average cosine of the downwelling light in the ocean under sea ice, given by $E_{0\downarrow}/E_d$, was seen to be independent of zenith angle. That higher zenith angles cause a larger relative change of heating rate (see also Table 2), is because the shape of the transmittance spectrum changes, with lower transmittance at longer wavelengths for higher zenith angles. When clouds are present similar changes in heating rate are found for varying zenith angles, but here the reason for the increase is that the clouds modify the incident spectrum, while the transmittance spectrum has the same shape regardless of zenith angle.

It was mentioned above that the snow and ice conditions essentially determine the average cosine of the light field directly below the ice. *Katlein et al.* [2014] showed that the light field under sea ice is more downward directed than what is demonstrated by most radiative transfer models, including the type used for this study. Hence, our simulations may show an average cosine for the light field under the ice that is underestimated. This could create a small bias toward absorption higher in the water column than what is actually the case. Quantifying the effect of preferred downward scattering in the sea ice is, however, difficult. It depends on the crystal structure of the ice, which varied considerably across the refrozen lead that was studied. Ice thickness may also influence the directional dependence of the under-ice light field.

It should also be noted that the model does not implement any spherical shell geometry, so for zenith angles approaching 90° the approximation of atmospheric mass becomes inaccurate. Up to about 80°, it is, however, a good approximation.

3.4. Time Series and Regional Scale Effects

By integrating the heating rate (Figure 3) over all wavelengths, and over depth, we get the energy absorbed in a layer, with units W m^{-2}. Figure 7 shows the absorbed energy for the upper 10 m of the water column, under thin ice (7a), thick ice (7b), and open water (7c). Curves for both cloud covered (cloud A) sky and clear sky are shown, and indicated by arrows in 7a are the IOP measurement profiles that are used in the other simulations. The data gap occurs during the relocation from floes 3 to 4; ac-9 profiles in May were collected on floe 3, while those in June were collected on floe 4. Ice and sky conditions are kept constant, so all variability is due to variability in measured IOPs.

We can clearly see that there are two different regimes prior to and after the bloom onset, and there appears to be less variability in the water column prior to the encounter with the bloom.

The above does not take into account changes in ice and snow properties, which for the refrozen lead that was studied caused large changes in transmitted irradiance. Between 18 May and 3 June, a general increase in transmittance was seen in the refrozen lead that was studied [*Kauko et al*., 2016]. On average, transmittance more than doubled between 26 May and 3 June. The model thin ice considered in this study, representative of the conditions on 26 May, has a transmittance of 0.17 under cloud A (Figure 1) and 0.15 without clouds (in the wavelength region considered), whereas the highest observed PAR transmittance was 0.4 [*Kauko et al*., 2016]. Relative to the effect of increased absorption and scattering in the water column the observed increase in transmittance is clearly dominating, in terms of added energy to the upper ocean.

Comparing Figures 7c to 7a and 7b, we see that the relative difference in absorbed energy between cloudy and clear skies is much larger when no ice and snow is present. This is again caused by multiple reflections between the surface and the clouds and atmosphere, which lead to an increase in the incident surface irradiance. With the same cloud properties (cloud A) and zenith angle, the incident surface irradiance on the thin ice with snow is about 40% higher than over open water. For cloud-free conditions, the radiation enhancement effect is much smaller, but backscattering from the atmosphere still gives incident irradiance that is 9% higher over the thin-ice surface with higher albedo. With clear skies, the incident irradiance is 274, 270, and 248 W m^{-2} on thick ice, thin ice, and open ocean, respectively. With cloud A, the corresponding values are 228, 213, and 150 W m^{-2}, a reduction of 17%, 22%, and 39%. As the albedo of the thick ice with thick snow is higher than the thin ice with snow (0.89 versus 0.78), this radiation enhancement effect is stronger over thick ice than over thin ice. Further, thicker clouds will increase the relative difference between open water and ice with snow due to higher degree of backscattering; incident irradiance over the thick ice cover with cloud B is more than 3 times higher than that over open water with the same

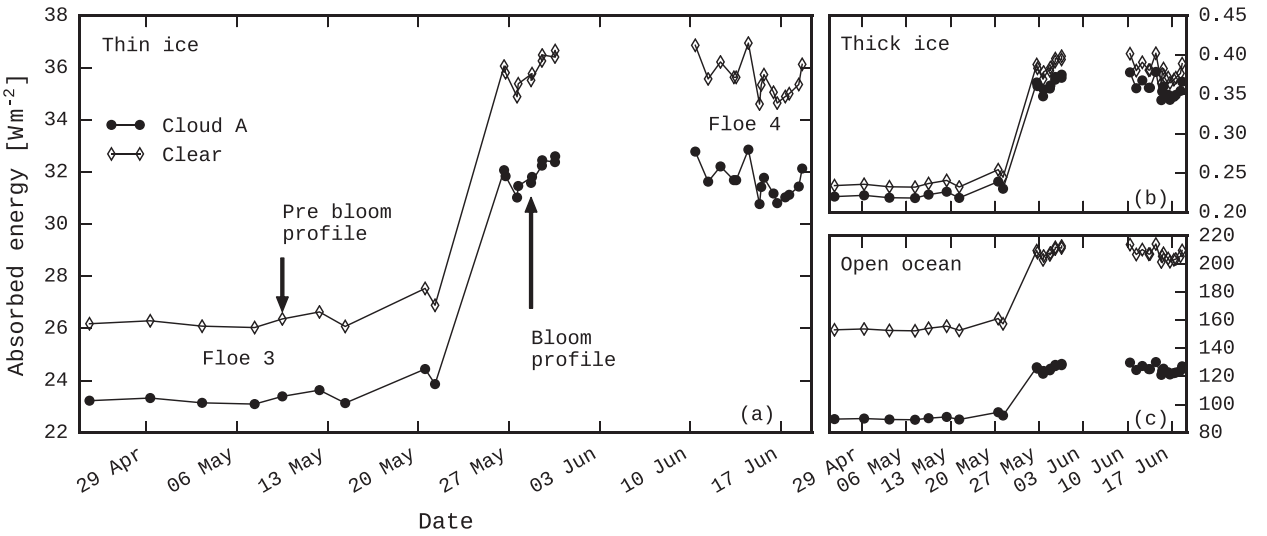

Figure 7. For each ac-9 profile (indicated by markers), the calculated absorbed energy in the upper 10 m of the ocean is plotted for (a) thin ice, (b) thick ice, and (c) open water conditions, with clear sky (open markers) and cloud A (filled markers). (Cloud A is a thin cloud case, cf. section 2.3.) Arrows in Figure 7a indicate the days on which the profiles shown in Figure 2 were collected. Ice conditions are kept constant throughout the time series in each case.

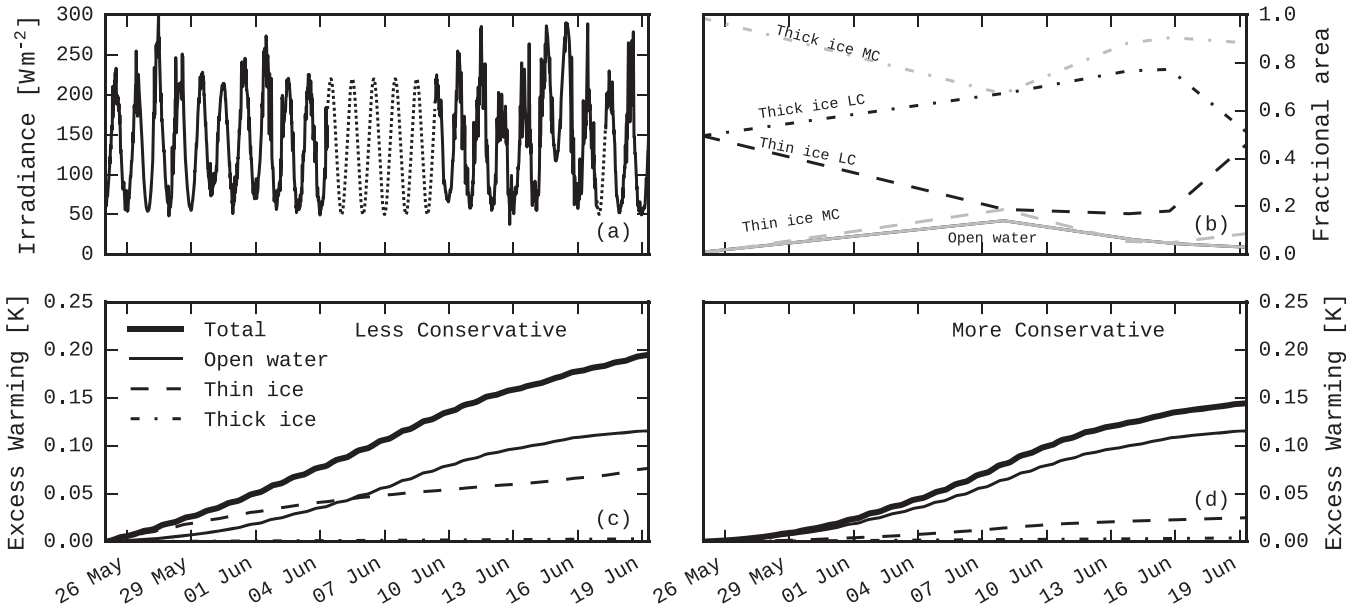

Figure 8. Time series of (a) incident irradiance; (b) areal fraction of ice types; (c, d) additional warming in upper 10 m due to the presence of the bloom, for two different estimations of ice type fractions. The dotted parts of the line in Figure 8a indicate where the gaps in the time series have been filled. "Total" is the sum of contributions from open water, thin ice, and thick ice. LC and MC in Figure 8b refer to, respectively, less and more conservative, which are different estimates for what is thick and thin ice. The open water fraction is the same in both cases.

clouds. For open leads in an otherwise ice-covered ocean, this effect will give higher incident irradiance than what a simulation with open water in a 1-D model such as AccuRT shows.

In order to estimate aggregate scale effects of the bloom on the warming of the upper layer, we calculate an accumulated warming over time, as follows. For each time step, the total warming ΔT of the water column down to a depth z' is calculated as

$$\Delta T = \sum_i \frac{E(t) \cdot \mathcal{T}_{i,\theta,w} \cdot \phi_{i,\theta,w,z'} \cdot \Gamma_i \cdot \Delta t}{\rho C_p \Delta z_i'}. \quad (3)$$

Here $E(t)$ is the measured incident irradiance at the time t, which is multiplied by the transmittance T for the ice type i (thick ice, thin ice, or open ocean), zenith angle θ and ocean IOPs w (prebloom or bloom conditions), to get downwelling irradiance at the ice bottom (or top of water column, for open ocean). ϕ is the fraction of downwelling light absorbed between the ice bottom and the depth z', and depends on zenith angle, water conditions, and ice type. Both T and ϕ are obtained from simulations done for varying zenith angles with the thin cloud layer, cloud A. Γ_i is the areal fraction of each ice type obtained from satellite images, and Δt is the length of the time step in seconds. To get the change in temperature for the whole layer, we divide by the density $\rho = 1028\,\mathrm{kg\,m^{-3}}$, the specific heat capacity of water $C_p = 4185\ \mathrm{J\,(kg\,K)^{-1}}$ and $\Delta z_i'$, the distance from the ice bottom to z'.

As mentioned previously, incident spectral irradiance was measured continuously on both floes 3 and 4 [*Taskjelle et al.*, 2016b]. For this exercise, the gap in the time series from 4 June to 9 June caused by the relocation, as well as a smaller gap in the time series from floe 4, was filled with a sine wave following the diurnal cycle (dotted parts of line in Figure 8a). Using satellite imagery of the area around the drift track, areal fractions of thin ice, thick ice, and open water were estimated (P. M. Wagner et al., Norwegian Meteorological Institute, 2016, personal communication) (Figure 8b). Two different estimates are considered, a less conservative (LC) estimate that has more thin ice and less thick ice, compared to the more conservative (MC) approach to classification. Open water fraction is the same for both approaches. We assume that the ice cases described above are representative for these three surface types. In using observed incident irradiance, we implicitly assume that there is no significant spatial variability of incident irradiance due to

reduced reflection between surface and clouds over narrow leads compared to the surrounding snow-covered ice.

Using equation (3), we calculate the cumulative warming from 25 May, when the bloom first was observed, to 19 June, when the time series of incident irradiance ends. Applying prebloom conditions to the whole period, the total energy absorbed in the upper 10 m for LC (MC) is 23 MJ m^{-2} (16 MJ m^{-2}), corresponding to a warming of 0.54 K (0.42 K). With bloom conditions, the total energy absorbed for LC (MC) is 31 MJ m^{-2} (23 MJ m^{-2}), giving a warming of 0.72 K (0.56 K). Hence, the additional warming of the upper 10 m due to the presence of the bloom over this 25 day period, shown in Figures 8c and d, is 0.19 and 0.14 K for LC and MC, respectively. In both scenarios, the areas of thick ice with thick snow have a minor contribution, while the open water areas contribute most to the additional warming. The additional energy accumulated in the upper 10 m is sufficient to melt 2.7 cm (2.0 cm) of pure ice for LC (MC), while the total potential ice melt due to solar heating of the upper 10 m is 10 cm (7.3 cm). These calculations do not take into account heat loss to the atmosphere from the open ocean, but as that would likely be similar regardless of the presence of the bloom, the results above will not be affected significantly.

Meyer et al. [2016] reported a mean mixed layer depth (MLD) of 6 m in the period from 25 May to the end of N-ICE2015, whereas before 25 May the MLD varied between 100 and 20 m, with a mean of 64 m. Using either 6 or 10 m as z' in equation (3), the bloom contributes about the same amount of additional energy deposition, 8.3 MJ m^{-2} (6.1 MJ m^{-2}) for LC (MC). With $z'=60$ m, representative of a deeper MLD, most of the solar energy is absorbed in the mixed layer regardless, so the effect of the bloom is only 0.25 MJ m^{-2} over the 25 days from 25 May to 19 June. Thus the concomitant changes in stratification and mixed layer depth play a significant role in the effect the bloom has on the heating of the upper ocean.

The aggregate scale mean of 31 MJ m^{-2} corresponds to an average heat flux to the upper 10 m of 14 W m^{-2} over the 25 day period, of which 4 W m^{-2} is due to the effect of the bloom. For comparison, the average vertical turbulent heat fluxes below the ice during floe 3 was 3.8 W m^{-2} [*Peterson et al*., 2016]. During floe 4, the average was 63 W m^{-2}, the higher value due in part to the passing of a storm.

4. Conclusion

We have investigated the effect of a phytoplankton bloom on the vertical distribution of solar radiant heating in the Arctic Ocean. Water absorption and attenuation coefficients prior to the bloom were found to be low compared to previous studies in the Arctic. The occurrence of a phytoplankton bloom led to a rapid increase in total water absorption and attenuation. Ratios of bloom to prebloom values were in the range 1.0–4.5 for absorption and 2.0–7.1 for attenuation, depending on wavelength. In contrast to prebloom conditions, the absorption and attenuation coefficients measured during the bloom were high compared to similar previous studies.

We considered three different types of surface conditions, open water, thin ice with a thin snow cover, and thick ice with thick snow, typical of the major ice types found in the region. As a result of the bloom, about 35% more energy was deposited in the upper 10 m of the water column. Over a 25 day period, we estimate that this could cause deposition of an additional 8.3 MJ m^{-2} of solar energy in the upper 10 m, sufficient to warm the water by as much as 0.19 K or melt 2.7 cm pure ice.

Acknowledgments
This work has been supported by the Norwegian Polar Institute's Centre for Ice, Climate and Ecosystems (ICE) through the N-ICE project, and the Research Council of Norway through the STASIS project (221961/F20). M.A.G., A.K.P., and S.R.H. were supported by the Polish-Norwegian Research Programme operated by the National Centre for Research and Development under the Norwegian Financial Mechanism 2009–2014 in the frame of Project Contract Pol-Nor/197511/40/2013, CDOM-HEAT. We would also like to thank our colleagues and the crews of R/V Lance for all assistance during the expedition. The data used in this study will be available through the Norwegian Polar Institute Data Centre (http://data.npolar.no). The AccuRT radiative transfer model is available for purchase from Geminor Inc. (sales@geminor.com).

References

Arndt, S., and M. Nicolaus (2014), Seasonal cycle and long-term trend of solar energy fluxes through Arctic sea ice, *Cryosphere*, *8*(6), 2219–2233, doi:10.5194/tc-8-2219-2014.

Arrigo, K. R., et al. (2012), Massive phytoplankton blooms under Arctic sea ice, *Science*, *336*(6087), 1408–1408, doi:10.1126/science.1215065.

Assmy, P., et al. (2016), Phytoplankton spring bloom beneath heavily snow-covered arctic sea ice during the N-ICE2015 cruise, in *Geophysical Research Abstracts EGU2016-17254*, vol. 18, EGU, Vienna.

Fortier, M., L. Fortier, C. Michel, and L. Legendre (2002), Climatic and biological forcing of the vertical flux of biogenic particles under seasonal Arctic sea ice, *Mar. Ecol. Prog. Ser.*, *225*(1), 16.

Granskog, M. A., A. K. Pavlov, S. Sagan, P. Kowalczuk, A. Raczkowska, and C. A. Stedmon (2015), Effect of sea-ice melt on inherent optical properties and vertical distribution of solar radiant heating in Arctic surface waters, *J. Geophys. Res. Oceans*, *120*, 7028–7039, doi:10.1002/2015JC011087.

Granskog, M., P. Assmy, S. Gerland, G. Spreen, H. Steen, and L. H. Smedsrud (2016), Arctic research on thin ice: Consequences of Arctic sea ice loss, *Eos Trans. AGU*, *97*, 22–26, doi:10.1029/2016EO044097.

Grenfell, T. C., and D. K. Perovich (1984), Spectral albedos of sea ice and incident solar irradiance in the southern Beaufort Sea, *J. Geophys. Res.*, *89*(C3), 3573–3580, doi:10.1029/JC089iC03p03573.

Hamre, B., S. Stamnes, J. J. Stamnes, and K. Stamnes (2014), AccuRT: A versatile tool for radiative transfer in coupled media like atmosphere-ocean systems, in *Ocean Optics XXII*, The Oceanography Society, Portland, ME. [Available at http://www.geminor.com/media/Hamre_OO2014_A0_portrait_v3.pdf.]

Hill, V. J. (2008), Impacts of chromophoric dissolved organic material on surface ocean heating in the Chukchi Sea, *J. Geophys. Res.*, *113*, C07024, doi:10.1029/2007JC004119.

Hill, V. J., and R. C. Zimmerman (2016), Characteristics of colored dissolved organic material in first year landfast sea ice and the underlying water column in the Canadian Arctic in the early spring, *Mar. Chem.*, *180*, 1–13, doi:10.1016/j.marchem.2016.01.007.

Hudson, S. R., M. A. Granskog, A. Sundfjord, A. Randelhoff, A. H. H. Renner, and D. V. Divine (2013), Energy budget of first-year Arctic sea ice in advanced stages of melt, *Geophys. Res. Lett.*, *40*, 2679–2683, doi:10.1002/grl.50517.

Hunter, J. D. (2007), Matplotlib: A 2D graphics environment, *IEEE Comput. Sci. Eng.*, *9*(3), 90–95, doi:10.1109/MCSE.2007.55.

Katlein, C., M. Nicolaus, and C. Petrich (2014), The anisotropic scattering coefficient of sea ice, *J. Geophys. Res. Oceans*, *119*, 842–855, doi:10.1002/2013JC009502.

Katlein, C., D. K. Perovich, and M. Nicolaus (2016), Geometric effects of an inhomogeneous sea ice cover on the under ice light field, *Front. Earth Sci.*, *4*(6), 10, doi:10.3389/feart.2016.00006.

Kauko, H., et al. (2016), Windows in Arctic sea ice: Light transmission and ice algal optical properties in a refrozen lead, *J. Geophys. Res. Biogesci.*, doi:10.1002/2016JG003626.

Lin, H., F. I. Kuzminov, J. Park, S. Lee, P. G. Falkowski, and M. Y. Gorbunov (2016), The fate of photons absorbed by phytoplankton in the global ocean, *Science*, *351*(6270), 264–267, doi:10.1126/science.aab2213.

Lotsberg, J., E. Marken, J. Stamnes, S. Erga, K. Aursland, and C. Olseng (2007), Laboratory measurements of light scattering from marine particles, *Limnol. Oceanogr. Methods*, *5*(1), 34–40, doi:10.4319/lom.2007.5.34.

Meyer, A., et al. (2016), Winter to summer hydrographic and current observations in the Arctic ocean north of Svalbard, *J. Geophys. Res. Oceans*, doi:10.1002/2016JC012391.

Mobley, C. D. (1994), *Light and Water: Radiative Transfer in Natural Waters*, Academic, San Diego, Calif.

Mobley, C. D. (2014), Gershun's Law, in *Ocean Optics Web Book*, NASA. [Available at http://www.oceanopticsbook.info/view/radiative_transfer_theory/level_2/gershuns_law.]

Mundy, C. J., et al. (2009), Contribution of under-ice primary production to an ice-edge upwelling phytoplankton bloom in the Canadian Beaufort Sea, *Geophys. Res. Lett.*, *36*, L17601, doi:10.1029/2009GL038837.

Pavlov, A. K., M. A. Granskog, C. A. Stedmon, B. V. Ivanov, S. R. Hudson, and S. Falk-Petersen (2015), Contrasting optical properties of surface waters across the Fram Strait and its potential biological implications, *J. Mar. Syst.*, *143*, 62–72, doi:10.1016/j.jmarsys.2014.11.001.

Pavlov, A. K., T. Taskjelle, H. Kauko, B. Hamre, S. R. Hudson, P. Assmy, P. Duarte, M. Fernández Méndez, C. J. Mundy, and M. A. Granskog (2016), Altered inherent optical properties and estimates of the underwater light field during an Arctic under-ice bloom of *Phaeocystis pouchetii*, *J. Geophys. Res. Oceans*, doi:10.1002/2016JC012471.

Pegau, W. S. (2002), Inherent optical properties of the central Arctic surface waters, *J. Geophys. Res.*, *107*(C10), 8035, doi:10.1029/2000JC000382.

Perovich, D. K. (2005), On the aggregate-scale partitioning of solar radiation in Arctic sea ice during the Surface Heat Budget of the Arctic Ocean (SHEBA) field experiment, *J. Geophys. Res. Oceans*, *110*, C03002, doi:10.1029/2004JC002512.

Peterson, A. K., I. Fer, M. G. McPhee, and A. Randelhoff (2016), Turbulent heat and momentum fluxes in the upper ocean under Arctic sea ice, *J. Geophys. Res. Oceans*, doi:10.1002/2016JC012283.

Petrich, C., M. Nicolaus, and R. Gradinger (2012), Sensitivity of the light field under sea ice to spatially inhomogeneous optical properties and incident light assessed with three-dimensional Monte Carlo radiative transfer simulations, *Cold Reg. Sci. Technol.*, *73*, 1–11, doi:10.1016/j.coldregions.2011.12.004.

Pope, R. M., and E. S. Fry (1997), Absorption spectrum (380–700 nm) of pure water. II. Integrating cavity measurements, *Appl. Opt.*, *36*(33), 8710–8723, doi:10.1364/AO.36.008710.

Röttgers, R., D. McKee, and C. Utschig (2014), Temperature and salinity correction coefficients for light absorption by water in the visible to infrared spectral region, *Opt. Express*, *22*(21), 25,093, doi:10.1364/OE.22.025093.

Smith, R. C., and K. S. Baker (1981), Optical properties of the clearest natural waters (200–800 nm), *Appl. Opt.*, *20*(2), 177, doi:10.1364/AO.20.000177.

Sogandares, F. M., and E. S. Fry (1997), Absorption spectrum (340–640 nm) of pure water I. Photothermal measurements, *Appl. Opt.*, *36*(33), 8699, doi:10.1364/AO.36.008699.

Taskjelle, T., M. A. Granskog, A. Pavlov, S. R. Hudson, and B. Hamre (2016a), N-ICE2015 total attenuation and absorption profiles from water column with AC-9 [Data set], Norwegian Polar Institute, doi:10.21334/npolar.2016.114bfaaa.

Taskjelle, T., S. R. Hudson, A. Pavlov, and M. A. Granskog (2016b), N-ICE2015 surface and under-ice spectral shortwave radiation data (v1.4) [Data set], Norwegian Polar Institute, doi:10.21334/npolar.2016.9089792e.

Thomas, G. E., and K. Stamnes (1999), *Radiative Transfer in the Atmosphere and Ocean*, Cambridge Univ. Press, Cambridge, U. K.

van der Walt, S., S. C. Colbert, and G. Varoquaux (2011), The NumPy array: A structure for efficient numerical computation, *Comput. Sci. Eng.*, *13*(2), 22–30, doi:10.1109/MCSE.2011.37.

Zaneveld, J. R. V., J. C. Kitchen, and C. C. Moore (1994), Scattering error correction of reflecting-tube absorption meters, in *Proc. SPIE 2258, Ocean Optics XII*, vol. 44, doi:10.1117/12.190095.